Centrosymmetric-noncentrosymmetric structural phase transition in the quasi-one-dimensional compound $(TaSe_4)_3I$

Arnab Bera,[1,*] Samir Rom,[2,*] Suman Kalyan Pradhan,[1] Satyabrata Bera,[1]
Sk Kalimuddin,[1] Tanusri Saha-Dasgupta,[2,†] and Mintu Mondal[1,‡]
[1]*School of Physical Sciences, Indian Association for the Cultivation of Science, Jadavpur, Kolkata 700032, India*
[2]*Department of Condensed Matter and Materials Physics, SN Bose National Centre for Basic Sciences, JD Block Sector III, Salt Lake, Kolkata-700106, India*

(Received 8 April 2023; revised 16 June 2023; accepted 26 June 2023; published 6 July 2023; corrected 2 August 2023)

$(TaSe_4)_3I$, a compound belonging to the family of quasi-one-dimensional transition metal tetrachalcogenides, has drawn significant attention due to a recent report on the possible coexistence of two antagonistic phenomena, superconductivity and magnetism below 2.5 K (Bera *et al.*, arXiv:2111.14525). Here, we report a structural phase transition of the trimerized phase at temperature $T \simeq 145$ K using Raman scattering, specific heat, and electrical transport measurements. The temperature-dependent single-crystal x-ray diffraction experiments establish the phase transition from a high-temperature centrosymmetric to a low-temperature noncentrosymmetric structure, belonging to the same tetragonal crystal family. The first-principles calculations find the aforementioned inversion symmetry-breaking structural transition to be driven by the hybridization energy gain due to the off-centric movement of the Ta atoms, which wins over the elastic energy loss.

DOI: 10.1103/PhysRevB.108.035112

I. INTRODUCTION

Symmetry plays a crucial role in dictating the properties of materials [1–4]. In particular, underlying crystal symmetry in reduced dimensions can have an important influence on their physical properties. Phase transitions accompanied by symmetry breaking in low-dimensional materials can endow fascinating phenomena [5–16]; for instance, ferroelectricity, associated with the loss of inversion symmetry [17,18], leads to spontaneous charge polarization. Similarly, in low-dimensional materials with broken inversion symmetry, spin-orbit coupling can result in novel spin textures and topological phases [19–22].

The family of transition metal tetrachalcogenides with generic formula $(MX_4)_nY$ (M = Nb, Ta; X = S, Se; Y = halogens like Br, I and $n = 2, 3, 10/3$) serve as a model *quasi*-1D system for studying a wide variety of phases and phase transitions [23–38]. These quasi-one-dimensional (quasi-1D) materials are composed of "M" atoms, surrounded by antiprisms of "X" atoms and arranged in 1D chain geometry, with "Y" ions between the chains giving cohesion. They are prone to Peierls instability and the filling of the metal d_z^2 band, given by $(n-1)/2n$, governs the nature of charge density wave (CDW) fluctuations driven by the correlation effect [25]. One member of the above family, $(TaSe_4)_2I$, is a chiral quasi-1D compound without an inversion center and has recently been claimed to be a topological Weyl semimetal, whose Weyl nodes are coupled with CDW modes, giving rise to an axion insulator [39–44]. This proposal opens up a novel avenue for investigating the interplay of strongly correlated CDW condensate and topology of electronic state, which may lead to the emergence of unusual quantum phenomena [16,39].

Another member of this family, $(TaSe_4)_3I$, has drawn attention in recent times due to a provocative report by some of us on the possible coexistence of ferromagnetism and superconductivity below 2.5 K [45]. The first experimental report by Roucau *et al.* in the 1980s [26] on $(TaSe_4)_3I$, showed that this compound is stabilized in crystal structure with space group $P4/mnc$ at room temperature, and exhibits weakly metallic behavior [26]. Despite being synthesized decades ago, the study on $(TaSe_4)_3I$ is found to be rather limited. Previous studies assumed that $(TaSe_4)_3I$ behaves similarly to $(NbSe_4)_3I$ due to their identical crystal structures [24–26]. However, the recent findings [45] demand separate attention to this compound, to understand the proposed exotic behavior. Theoretical calculations on $(TaSe_4)_3I$ [34] using the crystal structure derived from $(NbSe_4)_3I$ by replacing Nb with Ta, suggest the presence of a Van Hove singularity in the low-energy electronic structure of the material, which may contribute to its unique electronic properties. However, the origin of ferromagnetism coexisting with superconductivity remains elusive. The previous work [45] focused more on the properties of the low-temperature phase of $(TaSe_4)_3I$, while the details of the low-temperature phase as well as the possible structural phase transition were not comprehensively studied. On the other hand, to understand the exotic behavior found in our previous work [45], it is important to first understand the associated structural phase transition and details of the low-temperature crystal structure.

The present study aims to investigate the inversion symmetry-breaking structural phase transition observed in a

*These authors contributed equally to this work.
†t.sahadasgupta@gmail.com
‡mintumondal.iacs@gmail.com

quasi-1D compound, $(TaSe_4)_3I$, through a combination of experimental and theoretical approaches. The electronic transport, specific heat, and Raman-scattering experiments reveal a clear phase transition at around $T_S \sim 145$ K. The temperature-dependent single-crystal x-ray diffraction (SXRD) studies suggest that the phase transition is caused by a temperature-induced distortion of Ta chains that breaks the inversion symmetry at low temperatures, leading to a structural phase transition from a high-temperature (HT) centrosymmetric ($P4/mnc$) structure to a low-temperature (LT) noncentrosymmetric structure ($P\bar{4}2_1c$). We employ first-principles calculations together with *ab intio* derived tight-binding formulation to elucidate the microscopic origin of this inversion symmetry-breaking transition. The transition is found to arise from the gain in hybridization energy by the off-centric movement of Ta atoms, in the chainlike crystal structure, overpowering the elastic energy loss, akin to the mechanism of lattice-driven ferroelectricity. Our findings provide valuable insight into the unique symmetry-breaking structural transition in a quasi-1D system and will motivate further investigation of the impact of this symmetry-breaking structural transition on its physical properties.

II. EXPERIMENTAL AND CALCULATION DETAILS

$(TaSe_4)_3I$ single crystals were grown using the chemical vapor transport method with iodine as the transport agent, following the procedure described in detail in earlier work [45]. Temperature-dependent SXRD experiments were carried out on a Bruker D8 VENTURE microfocus diffractometer equipped with a PHOTON II detector, using Mo $K\alpha$ radiation ($\lambda = 0.710\,73^\circ$). The raw SXRD data were integrated and corrected for Lorentz and polarization effects using the Bruker APEX III program suite. Absorption corrections were performed using SADABS. The space groups were assigned by considering the systematic absences determined by XPREP and analyzing the metric symmetry. The space groups were further verified for additional symmetry using PLATON [46,47]. The crystal structure was solved by direct methods and refined against all data in the reported 2θ ranges by full-matrix least-squares refinement on F_2 using the SHELXL [48] program suite and the OLEX2 [49] interface.

Electronic transport measurements were carried out using a standard four-probe technique on a few ribbonlike oriented single crystals using a "Keithley 2450 source meter" in a Cryogenics 16 T measurement system. For the heat capacity measurement, a pallet was prepared by lightly pressing a bunch of single crystals in a palletizer. Specific heat measurements of an as-prepared pallet were done in a physical properties measurement system by Quantum Design. To uncover the nature of phase transition, Raman-scattering experiments were carried out on a single-crystal sample of $(TaSe_4)_3I$ across the phase transition temperature, $T_S \sim 145$ K using a 532-nm laser excitation in a Horiba T64000 Raman spectrometer (with spot size $\sim$1 μm).

The first-principles calculations were carried out with three different choices of basis sets: (a) plane-wave basis as implemented in the Vienna *Ab initio* Simulation Package (VASP) [50,51], (b) full potential linearized augmented plane wave (LAPW) as implemented in the WIEN2K code [52,53], and (c) linear and Nth-order muffin-tin orbital basis [54,55]. The consistency of the results in three different basis sets has been confirmed in terms of band structures and density of states plots. The exchange-correlation functional was chosen as a Perdew-Burke-Ernzerhof implementation of generalized gradient approximation. An $8 \times 8 \times 4$ Monkhorst-Pack k-point mesh was found to give good convergence of the computed ground-state properties. A plane-wave cutoff of 600 eV was used in plane-wave calculations with projected augmented wave potentials. For LAPW calculations, the criterion used was muffin-tin radius multiplied by $K_{\max}$ for the plane wave yielding a value of 7.0. The muffin-tin radii for the linear muffin-tin orbital (LMTO) calculations were chosen to be 3.06, 3.05, 3.32, and 2.50–2.60 Å for Ta (1), Ta (2), I, and Se, respectively in the case of a HT (300 K) structure, and 3.06, 3.06, 3.05, 3.30, and 2.55–2.70 Å for Ta (1), Ta (2), Ta (3), I, and Se, respectively, for the LT (100 K) structure. The plane-wave, LAPW, and LMTO calculations have been used to calculate the electronic structure both at HT and LT phases, to check the robustness of the semimetallic solution at HT and LT phases.

The construction of a low-energy Hamiltonian in first-principles derived Wannier function basis, for the purpose of evaluation of kinetic energy gain in the LT phase, was achieved through an Nth-order muffin-tin orbital (NMTO) downfolding technique starting from a full density functional theory (DFT) band structure. The NMTO calculations have been carried out with the potential obtained from self-consistent LMTO calculation. The real-space representation of the NMTO downfolded Hamiltonian, $H_{TB} = \sum_{ij} t_{ij}^{mm'}(C_{i,m}^{\dagger}C_{j,m'} + \text{H.c.})$, in the Wannier function basis gives the estimates of various hopping integrals (t) where m and m' are the non-downfolded orbitals at sites i and j, and $C_{i,m}^{\dagger}$ ($C_{j,m'}$) are electron creation (annihilation) operators.

III. RESULTS AND DISCUSSION

A. Phase transition at $T_S \simeq 145$ K

Figure 1(a) shows the measured temperature dependence of resistance [$R(T)$], and it decreases almost linearly with decreasing temperature (T). The obtained residual resistance ratio, $\frac{R_{300\,\text{K}}}{R_{2\,\text{K}}} = 30$, suggests that the sample is semimetallic. Additionally, the $R(T)$ curve shows a clear slope change at around 145 K (denoted by T_s), which is also evident in the dR/dT vs T plot (see upper inset) implying a phase transition. To get further insight into transport properties, we analyzed the temperature dependence of longitudinal resistance data using Matthiessen's rule [56,57].

$$R_{xx}(T) = R_0 + R_{e\text{-}p}(T) + R_{e\text{-}e}(T), \tag{1}$$

where R_0 is the residual resistivity arising from temperature-independent elastic scattering from static defects, $R_{e\text{-}p}$ represents the electron-phonon scattering contribution, which is proportional to T, while $R_{e\text{-}e}$ is the electron-electron scattering contribution proportional to T^2. The temperature dependence of $R(T)$ shows linear behavior in the temperature range 70–200 K, below and above the transition $T_S \sim 145$ K, suggestive of the dominance of the strong electron-phonon scattering mechanism in this temperature range. Below 15 K, R is found to vary quadratically with T [see lower inset

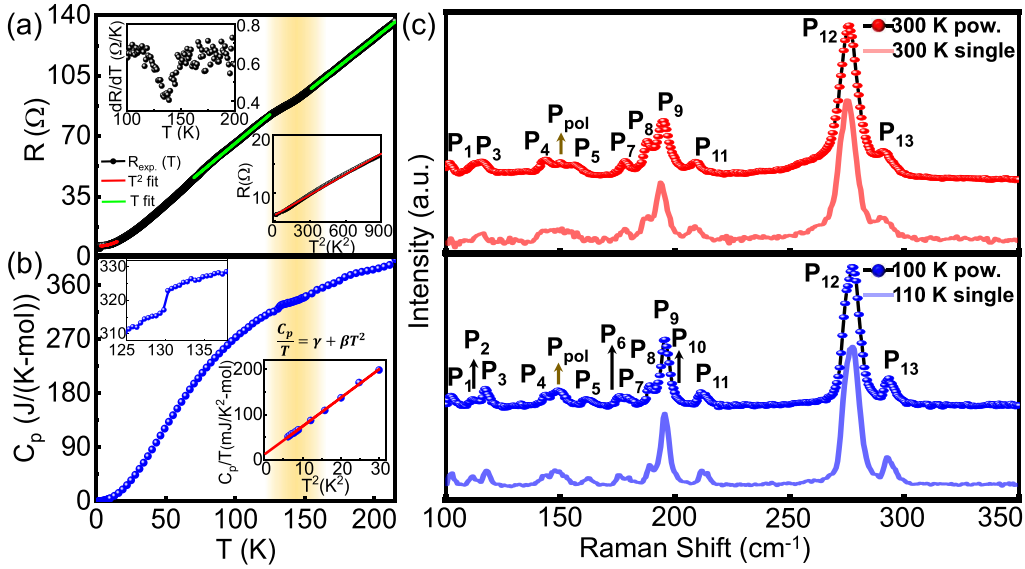

FIG. 1. Signature of phase transition in $(TaSe_4)_3I$: (a) Temperature-dependent resistance measurement of wirelike samples of $(TaSe_4)_3I$ down to $T \sim 2$ K. The upper inset (dR/dT versus T plot) shows the phase transition at around 145 K. Bottom inset: R vs T^2 plot in the 2.5–30 K range. The red solid line is a linear fit to the experimental data. (b) The specific heat data shows a sharp jump (zoom in, upper inset) which is a clear sign of a phase transition (the region presented in light yellow), at around $T_S \sim 145$ K. Lower inset: C_p/T vs T^2, exhibiting linear behavior at the low-temperature region. (c) Raman spectra of the powder as well as the single-crystalline sample at temperature $T = 300$ K (for both powder and single-crystal samples), $T = 100$ K (for the powder sample), and $T = 110$ K (for the single-crystalline sample). Arrows indicate the Raman-active modes P_2, P_6, and P_{10} that appear in the low-temperature sample below the transition.

in Fig. 1(a)], indicating a strong electron-electron scattering mechanism that dominates the transport properties in low-T regime [58]. No thermal hysteresis and significant change in T_S was observed during repeated cooling and heating cycles under a high magnetic field (H), implying the absence of any magnetic contribution.

To get further insight into this transition, we carried out temperature-dependent specific heat, $C_p(T)$ measurements of a pallet prepared using multiple (ribbonlike) single crystals in the temperature range 2.8–250 K. The aforementioned phase transition is manifested as a sharp change or steplike anomaly in C_p at $T \sim 140$ K [see Fig. 1(b)] [59]. It is to be noted, there is a slight difference in transition temperatures obtained from transport and specific heat measurements arising due to the use of samples with different geometry. To estimate the electronic contribution of specific heat (Sommerfeld coefficient) the $C_p(T)$ was analyzed using the equation $\gamma T + \beta T^3$ in the temperature range 2.5–6 K. inset of Fig. 1(b) shows the C_p versus T^2 plot for better clarity. γT represents the electronic contribution and βT^3 is the lattice contribution to the specific heat. The obtained Sommerfeld coefficients are $\gamma = 11.80$ mJ/K^2 mol and $\beta = 6.25$ mJ/K^4 mol. The large value of γ suggests the presence of a significant electronic correlation in the sample [60].

The probable structural phase is further studied through Raman spectroscopy. In order to cross-check the robustness of our findings we carried out measurements both in the single-crystal and in the powder sample. Figure 1(c) depicts the typical unpolarized Raman spectra of the powder sample of $(TaSe_4)_3I$ with prominent vibration modes in a spectral range of 100 cm$^{-1} < \omega < 350$ cm^{-1} at temperature $T \simeq 300$ K (RT) and 100 K (LT), respectively. For comparison, the Raman spectra for the single-crystal sample are also presented. We find very similar spectra for both the samples, apart from the fact that powder data allows us to resolve another Raman mode marked as $P_{\rm pol}$, which is present in both low-temperature and high-temperature spectra.

It is interesting to note that both powder and single-crystal data show the presence of three additional peaks, marked as the Raman-active modes P_2, P_6, and P_{10}. As the polarization factor can be ignored in the case of a powder sample, this clearly suggests the origin of additional peaks is different from polarization resolved peaks (see Fig. 7 in Appendix A2). Additionally, due to the low-temperature conditions, the Raman modes experience blueshifts, indicating an increase in mode frequency with decreasing temperature. Therefore, the appearance of three new peaks at an intermediate frequency at low temperatures cannot be attributed to the temperature effect alone, making the claim stronger that the structural phase transition may be responsible for the appearance of three additional peaks within the domain of scanned wave numbers [33,36,61–63]. The suggested phase transition as indicated in resistivity and specific heat data corroborated with Raman data, as well as its detailed nature, further confirm using temperature-dependent single-crystal x-ray diffraction (XRD), as presented below.

B. Confirmation of "structural phase transition": Broken inversion symmetry

The temperature-dependent single-crystal XRD studies were carried out to understand the structural changes across the phase transition.

TABLE I. SXRD refinement results for $(TaSe_4)_3I$ at $T = 100$ and 300 K.

Crystallographic information										
Temperature (T)	100 K					300 K				
Crystal system	Tetragonal					Tetragonal				
Space group	$P\bar{4}2_1c$					$P4/mnc$				
a (Å)	9.4358(5)					9.4696(5)				
b (Å)	9.4358(5)					9.4696(5)				
c (Å)	19.046(11)					19.049(11)				
$\alpha = \beta = \gamma$ (deg)	90					90				
Cell volume (Å^3)	1695.78					1708.19				
R factor (%)	2.27					2.75				
Atomic coordinates										
Atom	Site	x	y	z	B_{iso}	Site	x	y	z	B_{iso}
Ta(1)	4*d*	0.50	1	0.913	0.009	8*f*	0	0.50	0.58	0.021
Ta(2)	4*d*	0.50	1	0.573	0.009	4*d*	0	0.50	0.75	0.023
Ta(3)	4*d*	0.50	1	0.739	0.009	–	–		–	–
Se(1)	8*e*	0.547	0.785	0.820	0.011	16*i*	0.186	0.375	0.66	0.024
Se(2)	8*e*	0.313	0.876	0.832	0.011	16*i*	−0.048	0.28	0.672	0.025
Se(3)	8*e*	0.283	1.049	0.663	0.011	8*h*	0.021	0.275	0.50	0.026
Se(4)	8*e*	0.372	0.814	0.653	0.011	8*h*	−0.199	0.391	0.50	0.027
Se(5)	8*e*	0.610	0.800	0.493	0.012	–	–	–	–	–
Se(6)	8*e*	0.725	1.022	0.492	0.011	–	–	–	–	–
I	4*c*	0.50	0.50	0.626	0.022	4*e*	0.50	0.50	0.627	0.056

Crystal structure at $T = 300$ K. At room temperature $(TaSe_4)_3I$ crystallizes in tetragonal crystal structure (space group $P4/mnc$, No. 128). The lattice parameters of the $P4/mnc$ structure are found to be $a = b = 9.4696(5)$ Å, $c = 19.049(11)$ Å; $\alpha = \beta = \gamma = 90^\circ$. The complete details of the lattice constants, structural parameters, and R factors are listed in Table I. The RT crystal structure is shown in Fig. 2(a).

Key features of the RT crystal structure can be summarized as follows: (i) a unit cell of $(TaSe_4)_3I$ consists of parallel $TaSe_4$ chains, which are well separated from each other by I atoms as shown in Fig. 2(a). The iodine atoms provide cohesion to the structure, without active involvement in the bonding. (ii) There are 12 Ta atoms of two inequivalent classes, Ta(1) and Ta(2), in a unit cell. Each Ta atom is sandwiched between two nearly rectangular Se_4 units. The shorter Se-Se side of each Se_4 has a bond length of about 2.35–2.36 Å, a distance typical of a Se_2^{2-} dimer [25], while the longer Se-Se side is about 3.58–3.59 Å. Any two adjacent Se_4 units make an angle around 45°–50°. (iii) The Ta-Ta bonding along the chain exhibits the sequence of . . .-Short-Long-Long. . . (...S-L-L...) bonds. (iv) The distance between nearest $TaSe_4$ chains, $d_{inter} = 6.677$ Å, and the diameter of each $TaSe_4$ chain, $d_{intra} = 4.271$ Å. The distance between two opposite-faced $TaSe_4$ chains is 9.4 Å. This confirms the quasi-one-dimensional nature of the crystal structure with strong covalent bonds along the 1D chain direction, and weak interactions between the chains [25,64,65].

Crystal structure at $T = 100$ K. The SXRD experiment performed at $T = 100$ K reveals that low-temperature crystal structure also belongs to the tetragonal symmetry but with a different space group, $P\bar{4}2_1c$ (No. 114). Interestingly, the space group of the low-temperature crystal structure is noncentrosymmetric, in contrast to the centrosymmetric nature of the room-temperature $P4/mnc$ space group. Although, the refined lattice parameters of the LT phase: $a = b = 9.4358(5)$ Å, $c = 19.0464(11)$ Å; $\alpha = \beta = \gamma = 90^\circ$, are found to be similar to the lattice parameters of the crystal structure at RT. The complete crystallographic information is given in Table I. The obtained crystal structure corresponding to $T = 100$ K is presented in Fig. 2(b).

The essential features that capture the changes between the RT and LT crystal structures are summarized below.

(i) As mentioned above, the Ta-Ta bonding sequence along a $TaSe_4$ chain at RT structure is found to be a sequence of . . .-S (3.059 Å)-L (3.251 Å)-L (3.251 Å)-. . . bonds. The "L" bonds are formed between the Ta(1) and Ta(2) atoms and the "S" bonds are between both Ta(1) and Ta(1), and Ta(2) and Ta(2) atoms. On the other hand, the low-temperature structure [see Fig. 2(b)] exhibits a Ta-Ta bonding sequence of . . .-L (3.306 Å)-M (3.116 Å)-S (3.051 Å)-. . . bonds (M, medium). Compared to the HT structure, instead of two inequivalent Ta atoms, Ta(1) and Ta(2), three inequivalent Ta classes, Ta(1), Ta(2), and Ta(3) are formed in LT. The S, M, and L bonds are formed between the Ta(1) and Ta(2), Ta(2) and Ta(3), and Ta(1) and Ta(3) atoms, respectively. The Ta(3) atom is thus pulled closer to the Ta(2) atom so that the bond length between the Ta(2) and Ta(3) atoms is changed from L to M and the Ta(3)-Ta(1) bond length is increased slightly, compared to the HT structure (see Fig. 6).

(ii) As discussed, the individual chain is built by stacking of $TaSe_4$ antiprisms in a screwlike arrangement. The planes formed by both sides of the Se atoms are twisted with respect to each other at a certain "dihedral angle." Figures 2(c) and 2(d) show the sequence of dihedral angle at the HT structure and the LT structure. As is seen and as expected, the changes

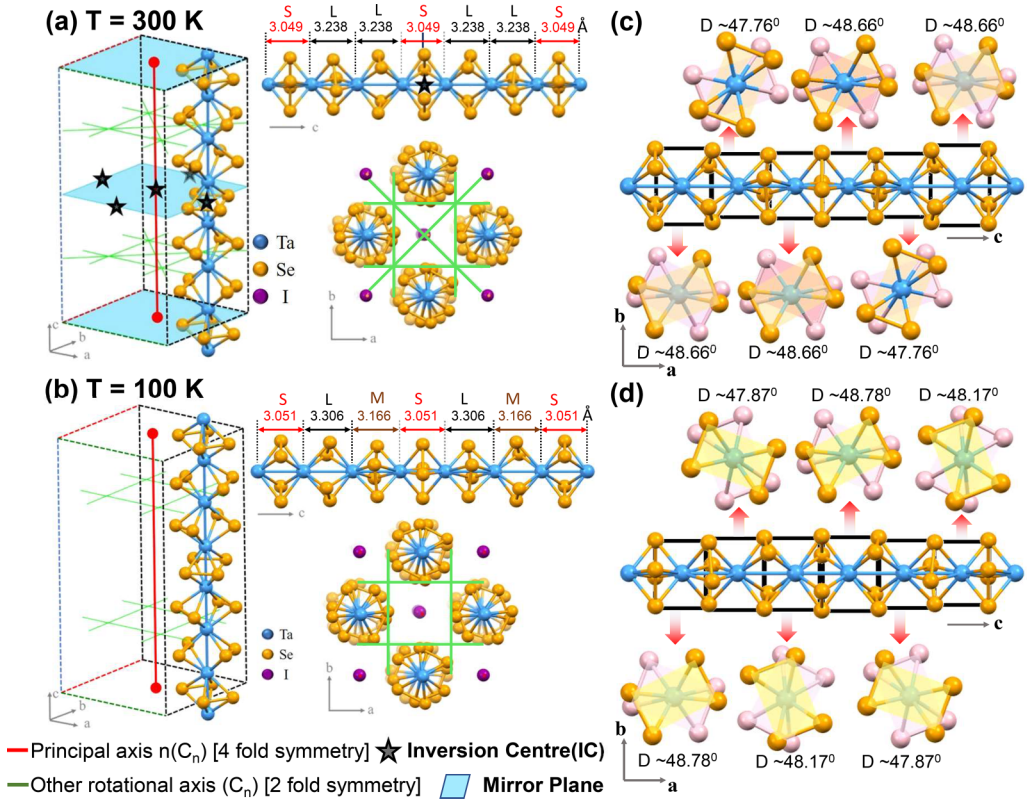

FIG. 2. Single-crystal XRDs: Structures and symmetries of $(TaSe_4)_3I$ single crystal. Schematic of the crystal structure of $(TaSe_4)_3I$, at (a) $T = 300$ K (RT) and (b) $T = 100$ K (LT). The "inversion center (IC)" points are highlighted with star symbols. The ICs only exist in the RT crystal structure. Similarly, mirror planes (shown in light blue) are visible in the crystal structure at RT, whereas they are absent in the LT crystal structure. For the simplification, different inequivalent Ta sites [Ta(1) and Ta(2) in HT and Ta(1), Ta(2), and Ta(3) in LT] are shown in the same color. (c),(d) The distribution of the dihedral angles in HT and LT (see text for details)

in the Ta-Ta bond sequence at the structural transition gets also reflected in dihedral angles.

(iii) Symmetry consideration yields the following major differences between the two structures:

(a) The RT structure hosts five inversion centers (ICs). Among them, four reside in the central position of each $TaSe_4$ chain, and the remaining one is at the center of the *tetragonal* unit cell [see Fig. 2(a)]. All five inversion centers are lost in the LT structure.

(b) The RT crystal structure also hosts mirror planes, whereas they are absent in the LT crystal structure [see Figs. 2(a) and 2(b)].

(c) Both RT and LT structures have one principal rotational axis [$n(C_4)$] that has fourfold symmetry. A careful look reveals the presence of a twofold rotational axis (C_2), which is six in RT structure and four in LT structure.

Temperature-dependent crystal structures. The temperature-dependent SXRD study confirms that there is an inversion symmetry breaking accompanied by a structural transition from a HT centrosymmetric phase to a LT noncentrosymmetric phase. Figures 3(a) and 3(b) show the temperature variation of bond distance between different Ta atoms and dihedral angles along the chains revealing the structural transition at around 145 K. The primary observations are as follows:

(a) With decreasing temperature, the bond distance between the Ta(1) and Ta(2) (S) sites remains similar throughout the entire temperature scan, whereas the distance between the Ta(3) and Ta(1) (L) and the Ta(2) and Ta(3) (L) sites follows a similar path down to 160 K. Below T_S, a slight shift of the Ta(3) atom along the chain changes the bond length between the Ta(2) and Ta(3) atoms from L to M; as a result, the Ta(3)-Ta(1) bond length increased slightly to keep the sum of bond lengths constant [see Fig. 3(a)]. These rearrangements of Ta atoms lead to the breaking of inversion symmetry in the crystal structure.

(b) The dihedral angle of the Ta(3) centered antiprism remains almost unchanged throughout the entire temperature variation while the dihedral angle of the Ta(1) and Ta(2) centered antiprisms behave in a similar manner down to 160 K. Below 160 K, the Ta(1) centered dihedral angle increases and the Ta(2) centered dihedral angle decreases with further lowering of the temperature [see Fig. 3(b)].

The temperature-dependent SXRD data (see Fig. 6 for more details on the structure) thus corroborate a unique centrosymmetric to noncentrosymmetric structural phase transition belonging to the same tetragonal symmetry in $(TaSe_4)_3I$, at around $T_S \sim 145$ K.

Identification of Raman modes and signature of structural transition. Having the confirmation of structural phase transition by SXRD, in this section we revisit the presence of additional Raman modes at LT, as described in Fig. 1(c), from the context of possible structural phase transition to a structure without inversion symmetry. Samples with no

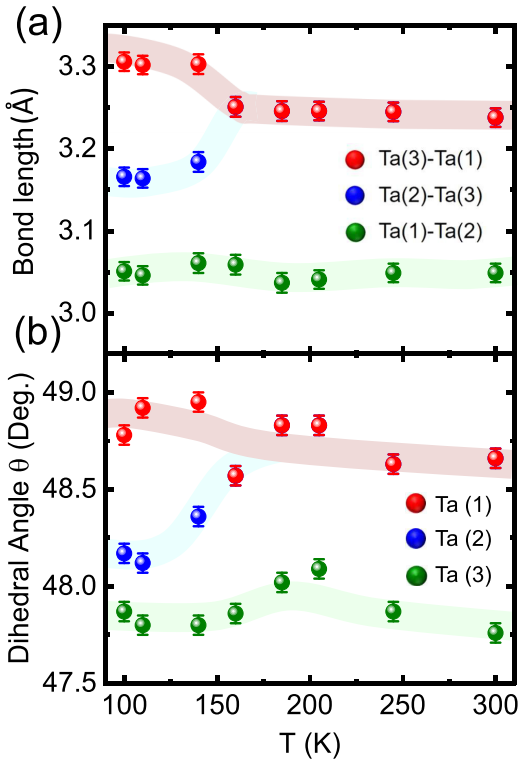

FIG. 3. (a) Temperature variation of bond distance among different Ta atoms and (b) dihedral angle. The solid sphere represents the experimental data, while thick solid lines are a guide to the eye.

inversion center have vibrational modes that are both Raman and infrared active, whereas those with an inversion center have zone-center lattice vibrations with even or odd parity [66,67]. Hence no normal modes can be both infrared and Raman active. The odd-parity vibration modes are Raman inactive due to selection rules, resulting in fewer Raman-active modes [61,66,67]. To determine the number of Raman-active modes for each phase, we conducted a group theory analysis.

Since the crystal structure changes across the phase transition at around 145 K, the group theory analysis allows us to determine the nature of each phonon mode by comparing their mode symmetry between two crystal phases (space group) as discussed below.

Centrosymmetric. The theoretical prediction of the vibration modes for a tetragonal crystal structure with space group $P4/mnc$ is described here according to lattice dynamics calculations. It is noteworthy to mention that there are 64 atoms in one unit cell (n) for both structures. The vibrational modes in the centrosymmetric phase differentiate into 192 ($3n$) mechanical representations, and can be represented as

$$\begin{aligned}\Gamma_{D4h} = &(A_{2u} + E_u) \\ &+ (12A_{1g} + 10A_{1u} + 13A_{2g} + 10A_{2u} \\ &+ 12B_{1g} + 10B_{1u} + 11B_{2g} + 9B_{2u} \\ &+ 27E_u + 24E_g). \end{aligned} \tag{2}$$

Among all these modes, three are acoustic, ($\Gamma_{D4h}^{\text{acoustic}} = A_{2u} + E_u$), and the remaining 189 modes are optical, ($\Gamma_{D4h}^{\text{optic}} = 12A_{1g} + 10A_{1u} + 13A_{2g} + 10A_{2u} + 12B_{1g} + 10B_{1u} + 11B_{2g} + 9B_{2u} + 27E_u + 24E_g$). In addition, among these optical modes, ($10A_{2u} + 27E_u$) are infrared (IR) active as well as Raman (R) inactive, While ($12A_{1g} + 12B_{1g} + 11B_{2g} + 24E_g$) shows the reverse characteristics (R active, but IR inactive).

Noncentrosymmetric. The vibrational modes corresponding to the noncentrosymmetric phase decompose into 192 mechanical representations, which can be depicted as

$$\Gamma_{D2d} = (B_2 + E) + (22A_1 + 22A_2 + 22B_1 + 21B_2 + 51E), \tag{3}$$

where the first and second groups of the representation correspond to the acoustic and optical modes, respectively. Here the IR-active and R-active modes are $\Gamma_{D2d}^{\text{optic}} = 21B_2 + 51E$ and $22A_1 + 22B_1 + 21B_2 + 51E$, respectively, among optical modes.

Notably, one important observation is that the number of Raman-active modes in the noncentrosymmetric phase (total 167 modes) is found to be greater than the centrosymmetric phase (total 83 modes), although the total number of vibration modes in both cases is identical. The three additional modes that appear in the Raman spectra of the low-temperature noncentrosymmetric phase, as shown in Fig. 1 due to the larger number of Raman-active modes predicted by the group theory analysis [61].

It is to be noted that in contrast to the above group theoretical analysis, we observed only a limited number of these modes. This can be attributed to some modes having weak photon-phonon coupling, which makes their detection challenging, or due to the laser excitation wavelength (we used 532-nm laser excitation). Similar to our data, Raman measurement on a similar sample of $(NbSe_4)_3I$ has also reported fewer Raman modes compared to the expected number of modes from group theory analysis [33]. Additionally, our experimental range is limited from 100 to 350 cm^{-1}. Expanding the wave-number range beyond this limitation may potentially reveal more Raman-active modes. However, due to the constraints of our experimental setup, it was not feasible to explore a wider range in this study.

C. Theoretical calculation

In order to uncover the origin of the structural transition, we carried out first-principles electronic structure calculations of $(TaSe_4)_3I$ at HT ($T = 300$ K) and LT ($T = 100$ K) crystal structures. The left panel of Fig. 4, shows the band structure of $(TaSe_4)_3I$ at 300 K, plotted along the high-symmetry k points of the tetragonal BZ and projected to Ta d and Se p states. As mentioned above, each Se_4 rectangle is made up of two Se_2^{2-} dimers. Each Ta atom in the $TaSe_4$ chain in the rectangular antiprism Se environment of Se atoms is thus in nominal 4+ or d^1 charge state. The electron withdrawal effect of iodine, present in between the chains, reduces the nominal valence of Ta from 4+, and makes it fractional to 4.333+ or $d^{2/3}$. As a linear chain with fractional occupancy, $f < 1$, leads to Peierls distortion, the $T = 300$ K structure shows trimerization with two inequivalent Ta atoms [Ta(1) and Ta(2)] and two L and one S Ta-Ta bond of sequence L-L-S…, as found in the experimentally measured structure. The Peierls distortion opens up a gap at the Fermi level, the magnitude of which

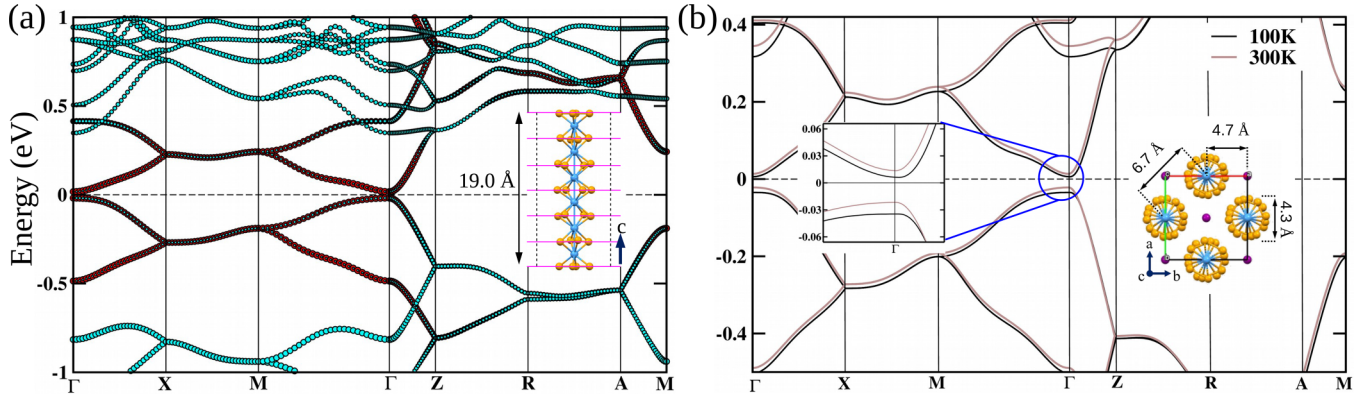

FIG. 4. (a) The band structure of $(TaSe_4)_3I$ at HT ($T = 300$ K) crystal structure, plotted along the high-symmetry k points, $\Gamma = (0, 0, 0)$-$X(\pi/a,0,0)$-$M(\pi/a, \pi/a,0)$-Γ-$Z(0, 0, \pi/c)$-$R(\pi/a, 0, \pi/c)$-$A(\pi/a, \pi/a, \pi/c)$-$M(\pi/a, \pi/a,0)$. The zero of the energy is set at the Fermi energy. The fatness of the bands indicates the orbital characters (red for Ta d, cyan for Se p). The inset shows the $TaSe_4$ chain running along the crystallographic c axis. (b) Comparison of the band structure for LT (100 K) crystal structure with that at RT (300 K). The change in the band gap between the two band structures is shown in the zoomed-in plot. The inset shows the $TaSe_4$ chains, separated by I atoms, in the $(TaSe_4)_3I$ structure, projected in the ab plane.

depends on the strength of the trimerization. Our calculated electronic structure shows a tiny gap of 0.02 eV, making the calculated electronic structure almost semimetal. From the projected orbital characters of the bands, it is seen that the low-energy band structure is dominated by Ta d, with some admixture from Se p. The rectangular antiprism coordination of Se atoms surrounding Ta, puts Ta $3z^2$-r^2 as the lowest energy state, which is about half-filled for Ta(1) and about empty for Ta(2). There are 12 Ta atoms in the unit cells, with 8 Ta(1) and 4 Ta(2), giving rise to eight Ta(1)-$3z^2$-r^2 dominated bands and four Ta(2)-$3z^2$-r^2 bands. The overlap between Ta(1)-$3z^2$-r^2 and Ta(1)/Ta(2)-$3z^2$-r^2 splits the eight Ta(1)-$3z^2$-r^2 dominated bands into a group of four occupied and four unoccupied bands, while the four Ta(2)-$3z^2$-r^2 bands remain more or less unoccupied. We find the bands are almost flat along X-M, i.e., going along the b direction, where two chains are separated by a distance of about 9.5 Å with intervening I^{-1} ions, which remain isolated (cf. insets). The occupied bands along M-Γ i.e., moving along the diagonal in the ab plane further splits due to Ta-Ta interaction via the intervening Se atoms of two neighboring chains (cf. insets). The trimerization along the chain direction, c, causes further band folding, as observed in the band structure along the Γ-Z direction. The basic features of the electronic structure of the 100-K crystal structure remain essential, the same as that of the high-temperature crystal structure (cf. right panel of Fig. 4 for comparison). Twelve Ta atoms in the unit cell are now split into three classes: four Ta(1), four Ta(2), and four Ta(3). The occupancies of Ta(1) and Ta(2) are found to be similar, being close to half-filled, while that of Ta(3) is found to be different, being more empty. We find that the band gap shows a tiny increase in the low-temperature phase from 0.02 to 0.03 eV, ensuring increased stability of the LT phase over the HT phase. It is worth mentioning here that the existence of the tiny but nonzero gap in the electronic structure of both HT and LT phases, as well as the enhancement of band gap value in the LT phase over the the HT phase have been confirmed by calculations in three different methods: plane wave, full potential LAPW, as well as LMTO. This makes the compound semimetal, as seen in the experiment.

In order to understand the origin of the HT-LT phase transition, we note that the low-temperature crystal structure, instead of the …L-L-S-L-L… sequence of Ta-Ta bonds in the chain of the HT phase adopt the …L-M-S-L-M… sequence (see the schematic diagram in Fig. 5). Thus the inversion symmetry at the center of the S bond at the HT phase, breaks down at the LT phase, making the transition akin to off-centric movement in ferroelectrics, with centrosymmetric HT and noncentrosymmetric LT crystal structures. The off-centric movement in ferroelectrics has been argued to arise from the gain in hybridization energy due to the distortion, balanced by the loss in elastic energy. In order to estimate the hybridization energy gain, we considered a Ta-$3z^2$-r^2–only model. We note

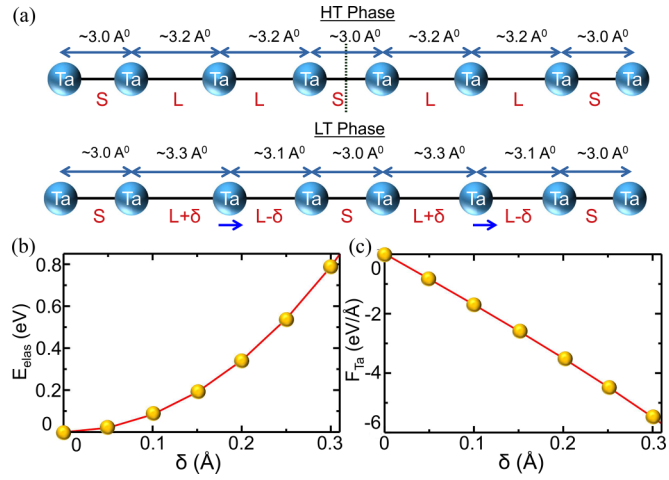

FIG. 5. (a) The schematic diagram of the distribution of Ta-Ta bond lengths in the $TaSe_4$ chain in HT and LT crystal structures. The center of inversion (marked as a dotted line) in the HT structure gets broken in the LT structure due to the distortion δ. Elastic energy (b) and force acting on Ta ions (c) plotted as a function of off-centric displacement (δ), obtained from DFT calculations.

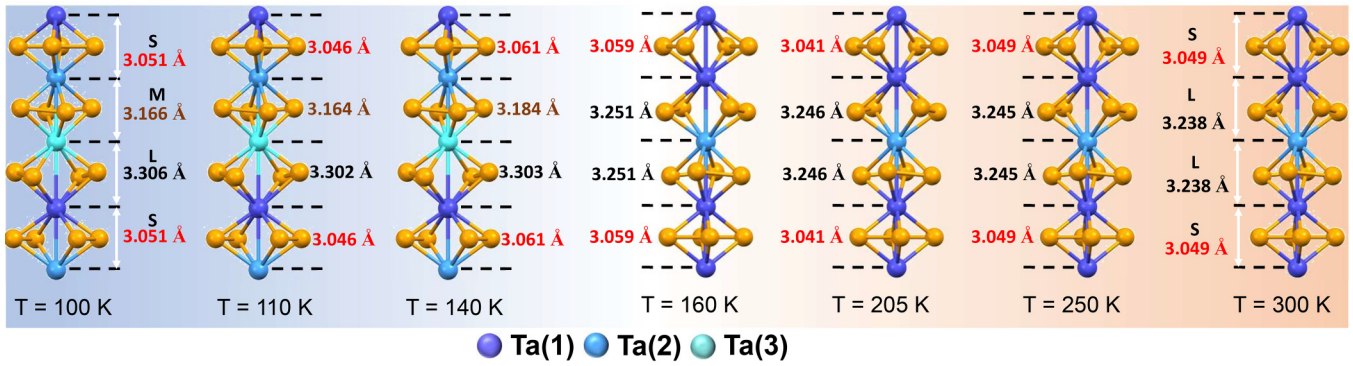

FIG. 6. Ta metal bonding sequence in *n*-TSI: Metal bonding sequence, obtained from SXRD data, along each $TaSe_4$ chain at $T = 100$, 110, 140, 160, 205, 250, and 300 K

that between the HT and LT structures, the S bond length remains more or less unchanged while the L bond at HT splits into ≈L+δ and ≈L-δ. We used the NMTO-downfolding method [55] to construct the Ta-$3z^2$-r^2–only model of the HT electronic structure, by integrating all the degrees of freedom, except Ta-$3z^2$-r^2 starting from the DFT band structure of the HT phase. The tight-binding Hamiltonian, constructed in the basis of the downfolded Ta-$3z^2$-r^2 Wannier function, provided the estimate of hopping, t_{dd}, corresponding to the L bond. The estimate of hopping, corresponding to the LT phase, was obtained by distance (l) -dependent scaling relation $t_{dd} \sim 1/l^{\beta}$ where $\beta = \partial ln t_{dd}/\partial ln l$. From the estimates of t_{dd} corresponding to the L and S bonds of the HT phase, β turned out to be ∼2. The kinetic energy gain due to additional off-centric distortion of the chain at LT over that in HT is thus given by

$$\Delta E_{KE} = -2t_{dd}^2(L+\delta) - 2t_{dd}^2(L-\delta) + 4t_{dd}^2.$$

The elastic energy cost due to two L bonds to L+δ and L-δ is given by

$$\Delta E_{\text{elas}} = \kappa \times \delta^2,$$

where κ is the stiffness constant. We estimated the stiffness constant from total energy calculations carried out on plane-wave basis upon varying values of δ. This is shown in Fig. 5. The stiffness constant can then be extracted by fitting the evolution of the energy as a function of δ with the function $f(\delta) = \kappa(\delta^2/2)$. We also adopted an alternative procedure of extracting the stiffness constant from the force acting on the Ta ions and fitting the data points with the function $f'(\delta)$. The two procedures gave rise to a similar value of κ16.8 eV/Å^2 from total energy and 17.0 eV/Å^2 from force estimate. Plugging in the values of t_{dd}, δ, and κ led to ΔE_{KE} of ∼− 0.03 eV, and $\Delta E_{\text{elas}} \sim 0.01$ eV, making the distorted LT structure more stable due to net hybridization energy gain. It is to be noted that the above simplistic analysis does not take into account the additional source of distortion, namely, the change in the dihedral angle between the Se rectangles. We also add that the above theoretical analysis is restricted to only one chain and the loss of the inversion center in the chain. Following the above analysis, one would expect $(TaSe_4)_3I$ to exhibit finite polarization. However, the experimentally determined $P\bar{4}2_1c$ (114) space group though noncentrosymmetric, is nonpolar as the corresponding point group $\bar{4}2m$ is nonpolar. This is caused by the additional loss of inversion in the center of the tetragonal cell in LT. The Ta-Ta bonding sequence in a given chain in the LT structure is . . .-L-M-S-. . ., while it changes to . . .-M-L-S-. . . in the neighboring chain. As checked explicitly, for identical bonding sequences between the chains, as in the HT structure, the LT space group would have been $P4nc$, with a polar point group, $4mm$, supporting the theoretical conjecture.

It is to be noted that although our calculation does not explicitly take into account the temperature effect, it makes an estimate of the hybridization energy gain and loss of the elastic energy, the interplay of which drives the temperature-driven structural phase transition. At low temperature, the gain overpowers the loss, thereby stabilizing the off-centric displaced structure. The temperature effect allows one to overcome the energy difference between elastic energy and hybridization energy, driving a phase transition, from a low-temperature off-centric displaced structure to a high-temperature undisplaced structure, very much like a ferroelectric to paraelectric transition. The difference between the hybridization energy gain and loss of the elastic energy is estimated to be 0.02 eV, which converted to temperature scale would be 232 K. Considering the simplistic approach of our calculation, which deals with only the single chain and the Ta-only model, neglecting interchain interaction and the effect of distortion of Se rectangles, and also does not take into account the entropic contribution, it is encouraging that the estimated temperature scale is in the same ballpark figure as the experimentally estimated structural transition temperature of ∼145 K.

IV. CONCLUSION

In summary, by employing a detailed analysis of the single-crystal XRD data, we have characterized the structural transition at around $T_s \sim 145$ K in $(TaSe_4)_3I$, evidenced in resistivity, specific heat, and Raman-scattering experiments. The structural transition turned out to be a symmetry-lowering transition of the trimerized Ta chains from the L-L-S sequence of Ta-Ta bonds to L-M-S Ta-Ta bonds, thereby breaking the center of inversion at the short Ta-Ta bond. This causes a transition between a high-temperature ($T > T_s$) centrosymmetric

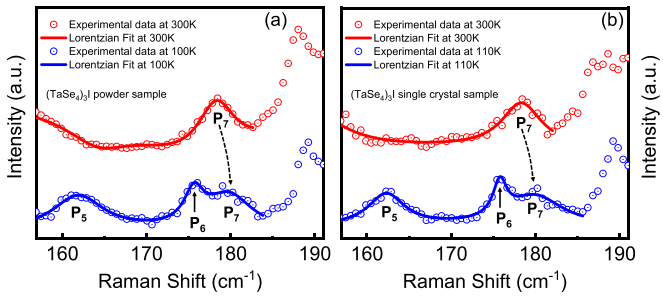

FIG. 7. Evaluation of the peak P_6 at low temperature: Raman spectra of single-crystal and powder samples clearly show that P_6 appears in the low temperature.

structure and a low-temperature ($T < T_s$) noncentrosymmetric structure belonging to the same tetragonal symmetry. The origin of this structural phase transition is examined in terms of first-principles DFT calculations and tight-binding modeling. We find the high- and low-temperature structures to both be semimetallic, consistent with the recent report. In terms of physical explanation of the experimental findings, our theoretical calculations find the following: (a) The microscopic origin of the centrosymmetric-noncentrosymmetric structural phase transition is the interplay of the hybridization energy gain and loss of the elastic energy, very much like that of the ferroelectric-paraelectric transition. First-principles derived estimates of the hybridization energy gain and elastic energy loss suggest that the hybridization energy gain wins over the elastic energy loss, thereby stabilizing the off-centric structure at low temperature and the undistorted, uniform structure at high temperature. The estimated temperature for the phase transition is in the same ballpark figure as the experimentally estimated temperature. (b) In spite of the above, the low-temperature structure remains nonpolar, although noncentrosymmetric, due to the additional loss of inversion in the center between different Ta-Ta chains. Our work opens up opportunities for exploring novel quantum phenomena in quasi-1D materials with broken inversion symmetry and could lead to the development of new quasi-1D materials with unique properties for potential applications. Our report of the centrosymmetric-noncentrosymmetric structural phase transition goes beyond well-studied charge-density-wave transition, opening up an entirely unexplored structural phase transition in this class of chain compounds.

ACKNOWLEDGMENTS

This work was supported by the Department of Science and Technology, Government of India (Grant No. SRG/2019/000674). A.B. thanks CSIR, Government of India for support from a research fellowship with Grant No. 09/080(1109)/2019-EMR-I. A.B. acknowledges the experimental facilities for sample growth, procured using financial support from DST-SERB Grant No. ECR/2017/002 037. T.S.-D. acknowledges JC Bose National Fellowship (Grant No. JCB/2020/000004) for funding. M.M. and A.B. would like to thank Atindra Nath Pal, Goutam Sheet, and Prabhat Mandal for the technical help and discussion. A.B. would like to acknowledge Mainak Palit for his technical help with Raman spectroscopy.

APPENDIX A: EVOLUTION OF STRUCTURE ACROSS TRANSITION

Figure 6 represents the thermal evolution of the Ta metal bonding sequence of a $TaSe_4$ chain obtained from SXRD data at various temperatures ranging from 100 to 300 K. At each temperature, the sequence of metal-metal bonds along the $TaSe_4$ chain was determined from SXRD data. The results reveal the temperature-dependent nature of the $TaSe_4$ chain structure as the temperature increases across the transition temperature, T_S.

APPENDIX B: EVOLUTION OF THE ADDITIONAL PEAK P_6 IN RAMAN SPECTRA

Figure 7 plots the evolution of peak P_6 as described in the main text. The plot clearly shows the appearance of P_6 in the low-temperature spectra. This is observed consistently in the powder and single-crystal samples. Note that the Raman modes experience blueshifts i.e., an increase in mode frequency with decreasing temperature, so the peak P_7 is slightly shifted towards a higher wave number at low temperature.

[1] J. Zak, Symmetry criterion for surface states in solids, Phys. Rev. B **32**, 2218 (1985).
[2] D. Gross, The role of symmetry in fundamental physics, Proc. Natl. Acad. Sci. USA **93**, 14256 (1996).
[3] L. Lederman and C. Hill, Symmetry and the Beautiful Universe (Prometheus Books, Buffalo, NY, 2007).
[4] L. Fu and C. L. Kane, Topological insulators with inversion symmetry, Phys. Rev. B **76**, 045302 (2007).
[5] N. P. Armitage, E. J. Mele, and A. Vishwanath, Weyl and Dirac semimetals in three-dimensional solids, Rev. Mod. Phys. **90**, 015001 (2018).
[6] F. Zhang, H. Min, M. Polini, and A. H. MacDonald, Spontaneous inversion symmetry breaking in graphene bilayers, Phys. Rev. B **81**, 041402(R) (2010).
[7] Y. Wang, G. Y. Cho, T. L. Hughes, and E. Fradkin, Topological superconducting phases from inversion symmetry breaking order in spin-orbit-coupled systems, Phys. Rev. B **93**, 134512 (2016).
[8] P.-P. Shi, Y.-Y. Tang, P.-F. Li, W.-Q. Liao, Z.-X. Wang, Q. Ye, and R.-G. Xiong, Symmetry breaking in molecular ferroelectrics, Chem. Soc. Rev. **45**, 3811 (2016).
[9] L. Du, T. Hasan, A. Castellanos-Gomez, G.-B. Liu, Y. Yao, C. N. Lau, and Z. Sun, Engineering symmetry breaking in 2D layered materials, Nat. Rev. Phys. **3**, 193 (2021).
[10] E. Wang, X. Lu, S. Ding, W. Yao, M. Yan, G. Wan, K. Deng, S. Wang, G. Chen, L. Ma, J. Jung, A. V. Fedorov, Y. Zhang, G. Zhang, and S. Zhou, Gaps induced by inversion symmetry breaking and second-generation Dirac cones

in graphene/hexagonal boron nitride, Nat. Phys. **12**, 1111 (2016).

[11] A. N. Berger, E. Andrade, A. Kerelsky, D. Edelberg, J. Li, Z. Wang, L. Zhang, J. Kim, N. Zaki, J. Avila, C. Chen, M. C. Asensio, S.-W. Cheong, B. A. Bernevig, and A. N. Pasupathy, Temperature-driven topological transition in 1T′-$MoTe_2$, npj Quantum Mater. **3**, 2 (2018).

[12] M. Bode, M. Heide, K. von Bergmann, P. Ferriani, S. Heinze, G. Bihlmayer, A. Kubetzka, O. Pietzsch, S. Blügel, and R. Wiesendanger, Chiral magnetic order at surfaces driven by inversion asymmetry, Nature (London) **447**, 190 (2007).

[13] V. Vescoli, F. Zwick, J. Voit, H. Berger, M. Zacchigna, L. Degiorgi, M. Grioni, and G. Grüner, Dynamical Properties of the One-Dimensional Band Insulator $(NbSe_4)_3I$, Phys. Rev. Lett. **84**, 1272 (2000).

[14] C. Pei, W. Shi, Y. Zhao, L. Gao, J. Gao, Y. Li, H. Zhu, Q. Zhang, N. Yu, C. Li, W. Cao, S. Medvedev, C. Felser, B. Yan, Z. Liu, Y. Chen, Z. Wang, and Y. Qi, Pressure-induced a partial disorder and superconductivity in quasi-one-dimensional Weyl semimetal $(NbSe_4)_2I$, Mater. Today Phys. **21**, 100509 (2021).

[15] D. Starešinić, P. Lunkenheimer, J. Hemberger, K. Biljaković, and A. Loidl, Giant Dielectric Response in the One-Dimensional Charge-Ordered Semiconductor $(NbSe_4)_3I$, Phys. Rev. Lett. **96**, 046402 (2006).

[16] S. Kim, Y. Lv, X.-Q. Sun, C. Zhao, N. Bielinski, A. Murzabekova, K. Qu, R. A. Duncan, Q. L. D. Nguyen, M. Trigo, D. P. Shoemaker, B. Bradlyn, and F. Mahmood, Observation of a massive phason in a charge-density-wave insulator, Nat. Mater. **22**, 429 (2023).

[17] P. W. Anderson and E. I. Blount, Symmetry Considerations on Martensitic Transformations: "Ferroelectric" Metals? Phys. Rev. Lett. **14**, 217 (1965).

[18] Y. Shi, Y. Guo, X. Wang, A. J. Princep, D. Khalyavin, P. Manuel, Y. Michiue, A. Sato, K. Tsuda, S. Yu, M. Arai, Y. Shirako, M. Akaogi, N. Wang, K. Yamaura, and A. T. Boothroyd, A ferroelectric-like structural transition in a metal, Nat. Mater. **12**, 1024 (2013).

[19] M. Sato and Y. Ando, Topological superconductors: a review, Rep. Prog. Phys. **80**, 076501 (2017).

[20] K. Matano, M. Kriener, K. Segawa, Y. Ando, and G.-q. Zheng, Spin-rotation symmetry breaking in the superconducting state of $Cu_xBi_2Se_3$, Nat. Phys. **12**, 852 (2016).

[21] L. Lu, Z. Wang, D. Ye, L. Ran, L. Fu, J. D. Joannopoulos, and M. Soljačić, Experimental observation of Weyl points, Science **349**, 622 (2015).

[22] Z. K. Liu, L. X. Yang, Y. Sun, T. Zhang, H. Peng, H. F. Yang, C. Chen, Y. Zhang, Y. Guo, D. Prabhakaran, M. Schmidt, Z. Hussain, S.-K. Mo, C. Felser, B. Yan, and Y. L. Chen, Evolution of the Fermi surface of Weyl semimetals in the transition metal pnictide family, Nat. Mater. **15**, 27 (2016).

[23] P. Monceau, J. Richard, and M. Renard, Charge-density-wave motion in $NbSe_3$. I. Studies of the differential resistance $\frac{dV}{dI}$, Phys. Rev. B **25**, 931 (1982).

[24] P. Gressier, A. Meerschaut, L. Guemas, J. Rouxel, and P. Monceau, Characterization of the new series of quasi one-dimensional compounds $(MX_4)_nY$ (M = Nb, Ta; X = S, Se; Y = Br, I), J. Solid State Chem. **51**, 141 (1984).

[25] P. Gressier, M. H. Whangbo, A. Meerschaut, and J. Rouxel, Electronic structures of transition-metal tetrachalcogenides $(MSe_4)_nI$ (M = Nb, Ta), Inorg. Chem. **23**, 1221 (1984).

[26] C. Roucau, R. Ayroles, P. Gressier, and A. Meerschaut, Electron microscopy study of transition-metal tetrachalcogenide $(MSe_4)_nI$ (M=Nb, Ta), J. Phys. C **17**, 2993 (1984).

[27] M. Izumi, T. Iwazumi, K. Uchinokura, R. Yoshizaki, and E. Matsuura, X-ray diffraction study of a structural phase transition in $(NbSe_4)_3I$, Solid State Commun. **51**, 191 (1984).

[28] A. Meerschaut, P. Gressier, L. Guemas, and J. Rouxel, Preparation and structure of $(NbSe_4)_{3.33}I$. $[I_3Nb_{10}Se_{40}]$, J. Solid State Chem. **51**, 307 (1984).

[29] A. Zwick, M. Renucci, P. Gressier, and A. Meerschaut, A Raman study of the Peierls transition in $(TaSe_4)_2I$, Solid State Commun. **56**, 947 (1985).

[30] M. Saint-Paul, P. Monceau, and F. Levy, Soft-acoustic-phonon mode at the phase transition in quasi-one-dimensional $(NbSe_4)_3I$, Phys. Rev. B **37**, 1024 (1988).

[31] I. Taguchi, F. Levy, and H. Berger, Metal-insulator transitions in the quasi-one-dimensional compound $(NbSe_4)_3I$, Physica B+C (Amsterdam) **143**, 258 (1986).

[32] T. Sekine, M. Izumi, and E. Matsuura, Raman scattering in linear-chain compounds $(NbSe_4)_{10/13}I$ and $(NbSe_4)_3I$, Synth. Met. **19**, 869 (1987).

[33] T. Sekine and M. Izumi, Successive phase transitions in the linear-chain semiconductor $(NbSe_4)_3I$ studied by Raman scattering and electrical resistivity, Phys. Rev. B **38**, 2012 (1988).

[34] I. Sánchez-Ramírez, M. G. Vergniory, C. Felser, and F. de Juan, Band structures of $(NbSe_4)_3I$ and $(TaSe_4)_3I$: Reconciling transport, optics and ARPES, Phys. Rev. B **107**, 205109 (2023).

[35] A. A. Balandin, F. Kargar, T. T. Salguero, and R. K. Lake, One-dimensional van der Waals quantum materials, Mater. Today **55**, 74 (2022).

[36] D. Dominko, S. Vdović, H. Skenderović, D. Starešinić, K. Biljaković, D. Ristić, M. Ivanda, J. E. Lorenzo, and J. Demsar, Static and dynamic properties of low-temperature order in the one-dimensional semiconductor $(NbSe_4)_3I$, Phys. Rev. B **94**, 104113 (2016).

[37] J. Kusz, M. Zubko, A. Prodan, H. J. P. van Midden, J. C. Bennett, and H. Böhm, The phase transition in the $(NbSe_4)_{10/3}I$ charge-density-wave system, Acta Crystallogr., Sect. A: Found. Crystallogr. **66**, s216 (2010).

[38] C. An, Y. Zhou, C. Chen, F. Fei, F. Song, C. Park, J. Zhou, H.-G. Rubahn, V. V. Moshchalkov, X. Chen, G. Zhang, and Z. Yang, Long-range ordered amorphous atomic chains as building blocks of a superconducting quasi-one-dimensional crystal, Adv. Mater. **32**, 2002352 (2020).

[39] J. Gooth, B. Bradlyn, S. Honnali, C. Schindler, N. Kumar, J. Noky, Y. Qi, C. Shekhar, Y. Sun, Z. Wang, B. A. Bernevig, and C. Felser, Axionic charge-density wave in the Weyl semimetal $(TaSe_4)_2I$, Nature (London) **575**, 315 (2019).

[40] X.-P. Li, K. Deng, B. Fu, Y. K. Li, D.-S. Ma, J. F. Han, J. Zhou, S. Zhou, and Y. Yao, Type-III Weyl semimetals: $(TaSe_4)_2I$, Phys. Rev. B **103**, L081402 (2021).

[41] W. Shi, B. J. Wieder, H. L. Meyerheim, Y. Sun, Y. Zhang, Y. Li, L. Shen, Y. Qi, L. Yang, J. Jena, P. Werner, K. Koepernik, S. Parkin, Y. Chen, C. Felser, B. A. Bernevig, and Z. Wang, A charge-density-wave topological semimetal, Nat. Phys. **17**, 381 (2021).

[42] Y. Zhang, L.-F. Lin, A. Moreo, S. Dong, and E. Dagotto, First-principles study of the low-temperature charge density wave phase in the quasi-one-dimensional Weyl chiral compound $(TaSe_4)_2I$, Phys. Rev. B **101**, 174106 (2020).

[43] Q.-G. Mu, D. Nenno, Y.-P. Qi, F.-R. Fan, C. Pei, M. ElGhazali, J. Gooth, C. Felser, P. Narang, and S. Medvedev, Suppression of axionic charge density wave and onset of superconductivity in the chiral Weyl semimetal Ta_2Se_8I, Phys. Rev. Mater. **5**, 084201 (2021).

[44] S. Ghosh, F. Kargar, N. R. Sesing, Z. Barani, T. T. Salguero, D. Yan, S. Rumyantsev, and A. A. Balandin, Low-frequency current fluctuations in quasi-1D $(TaSe_4)_2I$ Weyl semimetal nanoribbons, Adv. Electron. Mater. **9**, 2200860 (2023).

[45] A. Bera, S. Gayen, S. Mondal, R. Pal, B. Pal, A. Vasdev, S. Howlader, M. Jana, T. Maity, R. Ali Saha, B. Das, B. Satpati, A. Nath Pal, P. Mandal, G. Sheet, and M. Mondal, Superconductivity coexisting with ferromagnetism in a quasi-one dimensional non-centrosymmetric $(TaSe_4)_3I$, Res. Square (2021).

[46] A. L. Spek, Single-crystal structure validation with the program *PLATON*, J. Appl. Crystallogr. **36**, 7 (2003).

[47] A. L. Spek, Structure validation in chemical crystallography, Acta Crystallogr., Sect. D: Struct. Biol. **65**, 148 (2009).

[48] G. M. Sheldrick, A short history of *SHELX*, Acta Crystallogr., Sect. A: Found. Adv. **64**, 112 (2008).

[49] O. V. Dolomanov, L. J. Bourhis, R. J. Gildea, J. A. K. Howard, and H. Puschmann, *OLEX2*: A complete structure solution, refinement and analysis program, J. Appl. Crystallogr. **42**, 339 (2009).

[50] G. Kresse and J. Hafner, *Ab initio* molecular dynamics for liquid metals, Phys. Rev. B **47**, 558 (1993).

[51] G. Kresse and J. Furthmüller, Efficient iterative schemes for *ab initio* total-energy calculations using a plane-wave basis set, Phys. Rev. B **54**, 11169 (1996).

[52] P. Blaha, K. Schwarz, G. Medsen, D. Kvasnicka, J. Luitz, R. Laskowski, F. Tran, and L. Marks, *WIEN2k: An Augmented Plane Wave + Local Orbitals Program for Calculating Crystal Properties* (Karlheinz Schwarz, Techn. Universität Wien, Austria, 2018).

[53] P. Blaha, K. Schwarz, F. Tran, R. Laskowski, G. K. H. Madsen, and L. D. Marks, WIEN2k: An APW+lo program for calculating the properties of solids, J. Chem. Phys. **152**, 074101 (2020).

[54] O. K. Andersen, Linear methods in band theory, Phys. Rev. B **12**, 3060 (1975).

[55] O. K. Andersen and T. Saha-Dasgupta, Muffin-tin orbitals of arbitrary order, Phys. Rev. B **62**, R16219 (2000).

[56] N. V. Volkenshtein, V. P. Dyakina, and V. E. Startsev, Scattering mechanisms of conduction electrons in transition metals at low temperatures, Phys. Status Solidi B **57**, 9 (1973).

[57] B. Raquet, M. Viret, E. Sondergard, O. Cespedes, and R. Mamy, Electron-magnon scattering and magnetic resistivity in 3*d* ferromagnets, Phys. Rev. B **66**, 024433 (2002).

[58] A. H. Wilson, *The Theory of Metals* (Cambridge University Press, Cambridge, UK, 2011).

[59] M. Kratochvilova, A. D. Hillier, A. R. Wildes, L. Wang, S.-W. Cheong, and J.-G. Park, The low-temperature highly correlated quantum phase in the charge-density-wave 1T-TaS_2 compound, npj Quantum Mater. **2**, 42 (2017).

[60] L. Shulenburger, M. Casula, G. Senatore, and R. M. Martin, Correlation effects in quasi-one-dimensional quantum wires, Phys. Rev. B **78**, 165303 (2008).

[61] A. Bera, P. S. Rana *et al.*, Broken inversion symmetry in a quasi-1D compound $(TaSe_4)_3I$, investigated by Raman spectroscopy (unpublished).

[62] J. J. Gao, J. G. Si, X. Luo, J. Yan, F. C. Chen, G. T. Lin, L. Hu, R. R. Zhang, P. Tong, W. H. Song, X. B. Zhu, W. J. Lu, and Y. P. Sun, Origin of the structural phase transition in single-crystal $TaTe_2$, Phys. Rev. B **98**, 224104 (2018).

[63] K. Zhang, C. Bao, Q. Gu, X. Ren, H. Zhang, K. Deng, Y. Wu, Y. Li, J. Feng, and S. Zhou, Raman signatures of inversion symmetry breaking and structural phase transition in type-II weyl semimetal $MoTe_2$, Nat. Commun. **7**, 13552 (2016).

[64] P. Monceau, Electronic crystals: an experimental overview, Adv. Phys. **61**, 325 (2012).

[65] V. Favre-Nicolin, S. Bos, J. E. Lorenzo, J.-L. Hodeau, J.-F. Berar, P. Monceau, R. Currat, F. Levy, and H. Berger, Structural Evidence for Ta-Tetramerization Displacements in the Charge-Density-Wave Compound $(TaSe_4)_2I$ from X-Ray Anomalous Diffraction, Phys. Rev. Lett. **87**, 015502 (2001).

[66] R. Kakkar, *Atomic and Molecular Spectroscopy: Basic Concepts and Applications* (Cambridge University Press, Cambridge, UK, 2015).

[67] P. F. Bernath, *Spectra of Atoms and Molecules* (Oxford University Press, New York, 2016).

Correction: Two quantities appeared in the wrong locations in a description of terms following Eq. (1) and have been set right.